Controllable Li3PS4-Li4SnS4 solid electrolytes with affordable conductor and high conductivity for solid-state battery

Pingping Dong, Qing Jiao, Zengcheng Zhang, Miao Jiang, Changgui Lin, Xianghua Zhang, Hongli Ma, Baochen Ma, Shixun Dai, Tiefeng Xu

Controllable Li_3PS_4–Li_4SnS_4 solid electrolytes with affordable conductor and high conductivity for solid-state battery

Pingping Dong[1], Qing Jiao[1*], Zengcheng Zhang[1], Miao Jiang[3], Changgui Lin[1], Xianghua Zhang[2], Hongli Ma[2], Baochen Ma[1], Shixun Dai[1], Tiefeng Xu[4]

[1] Laboratory of Infrared Material and Devices, Advanced Technology Research Institute, Ningbo University, Ningbo 315211, China

[2] Laboratory of Glasses and Ceramics, Institute of Chemical Science, UMR CNRS 6226, University of Rennes 1, Rennes, France

[3] Ningbo Institute of Materials Technology and Engineering, Chinese Academy of Sciences, Ningbo, Zhejiang 315201, China

[4] Ningbo Institute of Oceanography, Ningbo 315832, China

Corresponding author: jiaoqing@nbu.edu.cn

Abstract High ionic conductivity, low grain boundary impedance, and stable electrochemical property have become the focus for lithium–sulfur solid–state batteries (ASSLSB). One of the approaches is to promote the rapid diffusion of lithium ions by regulating the chemical bond interactions within the framework. The structure control of P^{5+} substitution for Sn^{4+} on lithium-ion transport was explored for a series of Li_3PS_4–Li_4SnS_4 glass–ceramic electrolytes. Results showed that the grain boundary impedance of the glass electrolyte was reduced after

This article has been accepted for publication and undergone full peer review but has not been through the copyediting, typesetting, pagination and proofreading process, which may lead to differences between this version and the Version of Record. Please cite this article as doi: 10.1111/jace.18287.

heat treatments. The formation of LiSnPS microcrystals, a good superionic conductor, was detected by XRD tests. Electrochemical experiments obtained the highest conductivity of 29.5 S cm^{-1} at 100 °C and stable electrochemical window from – 0.1 V to 5 V at 25 °C. In addition, the cell battery was assembled with prepared electrolyte, which is promoted as a candidate solid electrolyte material with improved performance for ASSLSB.

Keywords: Sulfide solid electrolyte; Glass ceramics; Low grain impedance; All- solid-state batteries

Introduction

Electrochemical energy storage device such as Li second battery was believed to be the key technology for increasing requirement of pure electric vehicle, power backup device, and grid energy storage [1-6]. All-solid-state battery system was proposed to miniaturize the battery pack and improve the safety of battery [2]. Compared with the commercial Li^+ batteries, solid electrolytes exhibit comparable safe stability and energy density [2, 3]. Innovative sulfide electrolyte materials characterized by excellent ionic conductivity and wide stable electrochemical window have become the focus of ASSLSB. The sulfur solid electrolyte provided low elastic modulus and good formability due to its excellent ductility (Young's modulus=20 GPa), expecting that the bulk impedance is markedly decreased by cold pressing [4, 5]. Moreover, most solid sulfur electrolytes (SSE) can be proceeded by simply mechanical milling to avoid unnecessary reactions between active materials and SSE during hot sintering [6].

Recently the typical sulfide electrolyte material as $Li_{10}GeP_2S_{12}$ (LGPS) superionic conductor was explored by Kamaya et al. [7]. It provided a traditional three–dimensional framework structure and ensured effective lithium-ion transport channels. Moreover, the ionic conductivity is comparable with the commercial lithium batteries up to 12 mS cm^{-1}. However, Ge element as a raw material is relatively expensive and rare, limiting the commercialization of LGPS battery. Hence, high–conductivity, good electrochemical characteristics and low-cost SSE should be further explored [8-16]. Many researchers attempted to employ Sn or Si instead of Ge atom to construct similar structure for lithium-ion diffusion [17-25], which one of examples is the designed component of $Li_{10+\delta}[Sn_ySi_{1-y}]_{1+\delta}P_{2-\delta}S_{12}$ SSE [20]. Successfully controlled of element replacement, the increased lattice volume promoted the high ionic conductivity of $\sigma=1.1\times10^{-2}$ S cm^{-1} at 25 °C. When atoms with small radius are replaced by large ones, the ion transport framework expands to increase the volume of diffused lithium ions, thus facilitating lithium-ion conduction in channels. In the system of $Li_{10}Ge_{1-x}Sn_xP_2S_{12}$ SSE, the variation of conductivity decreases contrary to the increase in lattice volume due to the change of the combination bond on the potential energy of moving ions [26,27]. Therefore, the nature of substitution effect is a serious problem in the ionic transition for lithium-ion battery and must be further clarified.

In this work, the relatively cheap Sn element was used to completely replace the expensive Ge to explore the designed (1+*x*) Li_3PS_4–(2-*x*) Li_4SnS_4 SSE. The P/Sn ratio was adjusted to control of the crystal bones for evaluating the rule of lithium-ion transition. The conversion of PS_4 and SnS_4 structural tetrahedron allows the control of charge density surrounding Li^+

ions in the host framework. Ion's transport was discussed in terms of the potential energy of the coordination environment. The results obtained the glass–ceramics with high ionic conductivity 2.1 mS/cm and good electrochemical property after heat technology at room temperature (25°C). In addition, the battery LCO/2.5Li_3PS_4–0.5Li_4SnS_4/Li was assembled to evaluate the cycle performance. It enabled the exploitation of ASSLSB with desirable electrochemical properties, which revealed the expected superiorities of these devices.

2. Experiment

2.1 Material Synthesis

The sulfur solid electrolyte system of (1+*x*) Li_3PS_4–(2-*x*) Li_4SnS_4 (*x* =0, 0.5, 1, 1.5, 1.7) was synthesized through high energy mechanical ball milling and subsequent heat treatments. The initial materials including P_2S_5 (99 %, Aladdin), Li_2S (99.9 %, Aladdin) and SnS_2 (>99%, Aladdin) were weighed according to the ratio. The mixed initial feedstock (3g) was placed in a 45 mL ZrO_2 jar containing 12 ZrO_2 balls and ground at 510 rpm for 30h. Mechanical ball milling of *x* = 1.5 sample was selected for the heat treatment in a quartz ampule, with 500 °C, 550 °C, 600 °C, and 650 °C for 72h. The heating rate was 2.2 °C/min, and the cooling rate was 0.6 °C/min. All the preparations and sample treatments were proceeded in an Argon gas environment (O_2<0.1ppm, H_2O<0.1ppm), including the synthesis and electrochemical tests.

2.2 Structural Characterization

X-ray diffraction (XRD) test was performed using Bruker D2 Phase analyzer (10 mA, 30 kV) with Cu Kα radiation to determine the amorphous characteristic and crystalline state. Diffraction data was collected within the range of 10°–60 ° with 0.015° step size. A polymer film was used to prevent contact with air. Structural evolution was measured by Raman spectra equipped with an Ar ion laser (Renishaw In Via, Gloucestershine, UK) under the 488 nm excitation. Thermogravimetric/differential thermal (TG/DSC) (Germany, NETZSCH STA 449F3) was performed using a thermal analyzer at a heating rate of 10°C min^{-1} to determine the crystallization temperature (T_c). And the morphology of $2.5Li_3PS_4$-$0.5Li_4SnS_4$ samples before and after heat treatment was observed by SEM (SEM, JEOL, JSM-7001F).

2.3 Electrochemical Characterization

The impedance was measured using the AC impedance method in the Ar atmosphere by a Solartron electrochemical workstation (type: PGSTAT302N, Metrohm). The SE particles were cold-pressed at 180 MPa (diameter=10 mm, thickness= 0.8 mm). Stainless–steel (SS) sheets were then placed on either side of the electrolyte sheet as current collectors. Conductivity was calculated based on the equation $\sigma = D / (R \times A)$, D expresses the thickness, A denotes contact area, and R stands for the resistance of pellets. Electrochemical window was evaluated for solid electrolyte by cyclic voltammetry. SS and lithium metal were used as the cathode and anode of the cell, and measurements were conducted using the Solartron 1287 electrochemical interface with 1 mV s^{-1} scanning rate from –0.1V to 5V on an asymmetric Li/$2.5Li_3PS_4$–$0.5Li_4SnS_4$ SSE /SS cell.

All-solid-state battery $LiCoO_2$/$2.5Li_3PS_4$–$0.5Li_4SnS_4$ SSE/Li was prepared as follows. The cathode is comprised of $LiCoO_2$ (99.9% Sigma–Aldrich), the $2.5Li_3PS_4$–$0.5Li_4SnS_4$ SSE and conductive carbon. First, $LiCoO_2$, carbon black and $2.5Li_3PS_4$–$0.5Li_4SnS_4$ SSE with a ratio of 14:1:5 were weighted and ground in an agate mortar for 5 min. Then, the mixture (2mg) was pressed into the particle bulk at 180 MPa. After the $2.5Li_3PS_4$–$0.5Li_4SnS_4$ SSE (100 mg) was pressed into the particle bulk, the positive electrode was together pressed into double-layer particles under the same pressure. Finally, lithium foil was attached to one side of the double-layer particles with 90 MPa. The mixture served as the positive electrode, and lithium metal plate was regarded as the negative electrode. The $LiCoO_2$/$2.5Li_3PS_4$–$0.5Li_4SnS_4$ SSE/Li cell battery was thus assembled and tested for charge–discharge process in glovebox.

3. Result and Discussion

3.1. Structural Characterization

Fig. 1(a) displays the XRD patterns of samples after mechanical ball milling. Consistency was observed for all diffraction patterns, and several weak peaks near 19.8°, 29° and 46.5° indicated a crystallization tendency. Fig. 1(b) depicts the XRD pictures of the $2.5Li_3PS_4$–$0.5Li_4SnS_4$ SSE after heat treatments from 500 °C to 650 °C. All samples presented diffraction peaks at 14.2°, 19.7°, 20.1°, 26.4°, 29°, 36°, 40.7°, 46.5°, 50.7°, 51.2°, and 59.2°, which are in accordance with the crystalline phase of $Li_{10}SnP_2S_{12}$ [6, 17]. Also, the part diffraction peaks are consistent with Li_3PS_4 phase which peaked at 17°, 25.7°, 28.7°, 29°, 30.7°, 38.9°, 46.7°, 50.8°, respectively. It was indicated that the prepared electrolyte samples precipitated the high conductive phase similar to conductors Li_3PS_4 which contributed to the ions transport inside the network channels. Therefore, the sample structure was well

crystalized, and a similar tetragonal structure was formed within the precipitated crystals. Moreover, the overall diffraction peaks exhibited a trend of first increase and then decrease with heat treatment. When the temperature was raised to 550 °C, the XRD peaks became sharp and strong, revealing a high crystallinity was formed. However, the XRD peaks near 36° almost disappeared, and other peaks were weakened at 650 °C. It revealed that the optimal annealing temperature is 550 °C, which is hosted to the construction of network for lithium-ion transport. The crystallization temperature (T_c) of amorphized sample was measured by DSC to identify the optimum heat treatment temperature for glass-ceramics phases. As shown in Fig. S1 in the supplement file, the initial crystallization range of the $2.5Li_3PS_4$–$0.5Li_4SnS_4$ SSE sample is about 400-600 °C, which is basically selected as the heat treatment temperature range.

Raman test was conducted to clarity the framework of electrolyte after mechanical ball milling and heat treatments. In Fig. 2(a), the spectra of samples after milling show obvious peaks at approximately 380, 418 and 430 cm^{-1}. The peaks at 418 and 430 cm^{-1} were mainly caused by the stretching vibration of $\nu(PS_4)$ tetrahedrons [17]. And the vibration mode of $P_2S_6^{4-}$ units was contributed to the peak nearby 380 cm^{-1}. With increase of P substitution, these above peaks presented enhanced vibration intensity. However, the intensity of the peaks at 418 cm^{-1} and 430 cm^{-1} significantly declined when x=1.7, probably owing to the transformation of different structural sites of PS_4^{3-} tetrahedron [17, 28-32]. It indicated that PS_4^{3-} units were easier formed at x=1.5 and linked to restructure after further addition. As exhibited in Fig. 2(b), the Raman spectrum of LiSn(Ge)PS were almost consistent with previous reports [7,17, 30-32]. After continuous heat treatment of $2.5Li_3PS_4$–$0.5Li_4SnS_4$, the peaks intensity increased first and then descended as a whole. New peaks obviously appeared at 255, 285, 345, 405, 551 and 570 cm^{-1}, which of the peak at 345 cm^{-1} was ascribed to the vibration of SnS_4^{4-} tetrahedron [17, 33-34]. The peaks near 255, 418, 551, 570 cm^{-1} and the

broad asymmetric peaks in the 270–310 cm^{-1} range were mainly caused by PS_4^{3-} tetrahedron vibrations [17, 30-32], that exhibited a most connection of SnS_4 and PS_4 for the crystalline structure [17]. While the characteristic stretching vibrations of P−S bonds at 384 and 406 cm^{-1} were associated with the $P_2S_6^{4-}$ and PS_4^{3-} anions, respectively [30-32]. The enhanced vibration mode of PS_4^{3-} units at 418 cm^{-1} suggested that large Li^+ coordinated with sulfur involved in the ions transport process.

3.2. Ionic Conductivities

Fig. 3(a) presents the impedance plots of all samples after milling. The impedance of the samples decreases first and then increases with addition of P component. It was mainly attributed to the gradual increase of PS_4^{3-} tetrahedral structures identified by the Raman results. However, the conductive crystal structure was destroyed by the excess P when x= 1.7.

In this case, the Li^+ were most transported inside the non-crystal structure, leading to the increased impedance. Fig. 3(b) further provides the typical EIS profiles of $2.5Li_3PS_4$–$0.5Li_4SnS_4$ SSE with different heat treatments. Impedance diagrams are usually composed of semicircular arcs and oblique lines (electrode grain and grain boundary) [17, 24]. Herein, the lacked semicircle with only one slope at 550 °C was observed, indicating that the contribution of the grain resistance from semi-circular arc is almost negligible. With increase of heat temperature, the value of the impedance decreases first and then increases obtaining the minimum impedance of 50Ω, when the temperature increased to 650 °C, the impedance value then increased which of the result was in accordance with Raman analysis that the declined PS_4 unit as conducive to lithium ions. It has been reported by Tatsumisago M. that a heat-treated Li_2S–P_2S_5 glass-ceramic conductor realized an extremely high ionic conductivity

of 1.7 x 10^{-2} S cm^{-1}. The optimum conditions of the heat treatment reduced the grain boundary resistance and the influence of voids, increasing the Li^+ ionic conductivity of the solid electrolyte [35]. Also, SEM pictures before and after heat treatment of $2.5Li_3PS_4$–$0.5Li_4SnS_4$ was supplemented in Fig. S2. For $2.5Li_3PS_4$–$0.5Li_4SnS_4$, a small number of crystals were precipitated after ball milling, and the whole electrolyte was still in the glass state with tendency of phase separation. After 550 °C heat treatment, a large number of crystals were precipitated, the contact between grains was closer and the density was intensified, which reduced the grain boundary impedance and improved the ionic conductivity. In addition, the EDS spectra in supplement display the elements are uniformly distributed inside the sample before and after heat treatment, even better after heat treatment. Therefore, it was believed that the conductivity was optimized by modification of the electrolyte component and further heat influence. Fig. 3(c) displays the ionic conductivity at different x values after mechanical ball mill and different heat treatment temperatures, where the maximum ionic conductivity of $2.5Li_3PS_4$–$0.5Li_4SnS_4$ SSE at 550℃ was 2.1×10^{-3} S cm^{-1}.

Electronic conductivity can be calculated by the formula $\sigma_e = DI/SE$, where D is the sample thickness, S represents the contact area, E expresses the polarization voltage, and I is the electronic current. A difference of seven orders of magnitude was found between electron conductivity and ionic conductivity exhibit in Fig. 3(d). Therefore, the electronic conductivity $\sigma_e=1.02 \times 10^{-9}$ S cm^{-1} was almost negligible, implying that the grain conductivity contributes to the fast Li^+ transport and is not caused by electronic conduction. Fig. 3(e) displays the impedance value of $2.5Li_3PS_4$–$0.5Li_4SnS_4$ SSE along with the temperatures, which was high

up to 29.5 mS cm^{-1} at 100 °C. Accordingly, the ionic conductivity showed good fitting on the basis of the Arrhenius Law. As shown in Fig. 3(f), the activation energy (Ea) values were calculated as 0.335 eV, 0.325 eV, 0.332 eV, 0.336 eV, respectively at 500-650 °C. The results showed that the activation energy was low to about 0.325 eV when heat treated at 550 ℃, which is a relatively low value compared with the result of the result of $Li_{10}SnP_2S_{12}$ (0.31eV) reported by Bron P. [24]. When the heat treatment temperature was properly controlled, crystal impedance was reduced, and ionic conductivity was enhanced. Consequently, the binding ability of sulfur atoms (P-S bond) could be adjusted to the nearby Li^+ by optimization of Sn/P ratio in response to the migration of lithium ions [26, 27].

3.3. Cyclic Voltammetry

According reports, there is usually a narrow electrochemical window (about 1.8~2.3 V vs Li^+/Li) for chalcogenide solid electrolytes such as $Li_{10}GeP_2S_{12}$ [12]. Fig. 4 evaluated the electrochemical stability of $2.5Li_3PS_4$–$0.5Li_4SnS_4$ SSE by Cyclic Voltammetry (CV) in Ar atmosphere. The assembled battery adopted the stainless steel and lithium applied for the poles of working electrode. No significant redox reaction occurred at –0.1 to 5 V in CV curve, except for oxidation and reduction peaks at approximately 0 V (vs Li/Li^+), which were attributed to the lithium ions dissolution $(Li \rightarrow Li^+ + e^-)$ and deposition $(Li^+ + e^- \rightarrow Li)$ [15]. It was believed that good electrochemical stability was obtained and the electrochemical window high up to 5V was realized.

4. Structural Model of Li^+ Transportation

It is suggested that Li^+ diffusion depends on the potential energy surface which of the distribution is decided by the interaction between the movable Li^+ and the matrix including the electrostatic interaction between Li^+ ions [26, 27]. As depicted in Fig. 5(a), the quadrilateral frame structure $Li_{10}SnP_2S_{12}$ was composed of SnS_4^{4-} and PS_4^{3-} tetrahedral anions containing interstitial-state Li^+ ions. The main frame structure provides channels for ion migration along the c direction, and Li^+ alternately moves through Li(1) and Li(3) sites (Fig. 5(b)), leading to the rapid ions diffusion [6, 19, 23]. In addition to the effect of structure control on electrical conductivity, the nature of the chemical environment around Li ions also influences its migration. Krauskopf proposed an idea for solid–electrolyte inductive impact, in which the bonding changes of the host frame in solid electrolyte modified the potential energy pattern of the mobile ions [26, 27]. In the crystal ceramic structure, the S atoms in the M–S (M=P, Sn) bonds are arranged on both sides of the c access channel. The polarity of Sn-S bond is greater than that of the equivalent P-S bond as schematized in Fig. 5(c). Therefore, the negative charge density of P-S atom was decreased indicating that the electrostatic of S···Li interaction is lower than that of Sn analogue in the P-substituted system. The efficiently reduced energy barrier of lithium–ion diffusion along channels improved the conductivity of Li^+ and optimized electrochemical performance [26, 27].

5. All solid - state battery

A prototype cell of $2.5Li_3PS_4$–$0.5Li_4SnS_4$ SSE in ASSLSBs was assembled in Fig. 6(a). Fig. 6(b) shows the cyclic performance including the columbic efficiency from 3V to 4.2V

and the current density of 40 mA/g of the battery. Compared with the theoretical capacity of lithium cobalt oxide at 120 mA h/g, the first cycle discharge capacity was activated for 93 mA h/g and the charging capacity reached at 102.8 mA h/g. In addition, the coulomb efficiency was 90.5%, and the discharge capacity accounted for 77.5% of the theoretical capacity, which of these values performed relatively good electrochemical properties. As the cycle goes on, the discharge capacity after 20 cycles was retained at 73.2 mA h/g, and the capacity retention rate was maintained at 78.7%. The coulomb efficiency always outperformed at 99.5%, indicating that the cell possesses good reversibility for lithium-ion transport. The charge/discharge capacity during cycling is displayed in Fig. 6(c). The discharging platform was approximate 3.7 V, and the charging platform was relatively long and distributed between 4 V and 4.2 V. In order to explore the reason of capacity fading with assembled LCO/2.5Li_3PS_4–0.5Li_4SnS_4/Li battery, we carried out impedance tests after the first and the 25th cycles. As shown in Fig. 6(d), R_{bulk}, $R_{interface}$ and ZW are SSE resistance, interface resistance (cathode/electrolyte) and diffusion impedance in equivalent circuit diagram, respectively. R_1 is the SEE impedance and R_2 reflects the total impedance of the battery (SSE and Electrode interface resistance). After 25 cycles, the electrode interface impedance (R_2-R_1) [37-38] increased about 25Ω. As previous reported [39-40], the change of interface resistance between cathode and electrolyte was much larger than that between electrolyte and lithium [41-42]. Thus, the variation of the interfacial resistance was mainly attributed to the continuous shuttle effect of Li^+ ions at the electrolyte and cathode interface during cycling, which lead to the contact failure between cathode and solid electrolyte. Hence, stable interface contact is crucial for ASSLSB with good cycling performance.

6. Conclusions

Glass–ceramic (1+x) Li_3PS_4–(2-x) Li_4SnS_4 SSEs were successfully synthesized through mechanical ball milling and continuous heat treatments. The resistance of the grain boundary was effectively reduced by controlling P/Sn ratio and heat treatments. Owing to the less electronegativity of P than Sn, the weak coulomb attraction between S and nearby Li^+ cations was formed. Thus, Li^+ was transported faster in the designed channel, and the ionic conductivity was significantly improved. When the heat temperature reached 550 °C, the obtained $2.5Li_3PS_4$–$0.5Li_4SnS_4$ SSE showed the higher ionic conductivity (2.1×10^{-3} S cm^{-1}) and lower E_a with 0.325 eV. Furthermore, the constructed ASSLSB delivered a wide and stable electrochemical window from –0.1 V to 5 V. A good cyclic performance was attained with capacity retention rate kept at 78.7% and the coulomb efficiency always outperformed 99.5%. The work improved the understanding of effect on the chemical bond energy of structure–property relationships in ionic conductors. It paved the way for the enhancement of ionic conductivity in SSE and the acceleration of all-solid-state battery applications.

Acknowledgement

This work was financially supported by National Natural Science Foundation of China (Grant no. 51972176) and sponsored by K. C. Wong Magna Fund in Ningbo University.

References

1. Liu Z, Fu W, Payzant E A, Yu X, Wu Z L. Dudney, N. J.; Kiggans, J. Anomalous High Ionic Conductivity of Nanoporous β-Li_3PS_4. J. Am. Chem. Soc. 2013; 135: 975-978.

2. Rajagopala R, Ryu K S. Evaluation of $Li_6P_2S_8I$ Solid Electrolyte for All Solid-State Lithium Battery Applications. Chem. Eng. J. 2020; 402: 3065-3071.

3. Yi J, Chen L, Liu Y, Geng H, Fan L. High Capacity and Superior Cyclic Performances of All-Solid-State Lithium-Sulfur Batteries Enabled by a High-Conductivity $Li_{10}SnP_2S_{12}$ Solid Electrolyte. ACS Appl. Mater. Interfaces. 2019; 11: 36774-36781.

4. Shan Z, Wang H, Wang Y, Shen Y, Zhang J, Chen Y, Zheng Q, Zhang Y, Tao H. Mixed Alkaline Earth Effects on Crystallization Behavior of Basalt Glasses and Liquids. J. Alloys Compd. 2021; 874: 159986.

5. Kraft M A, Ohno S, Zinkevich T, Koerver R, Culver S P. Inducing High Ionic Conductivity in the Lithium Superionic Argyrodites $Li_{6+x}P_{1-x}Ge_xS_5I$ for All-Solid-State Batteries. J. Am. Chem. Soc. 2018; 140: 16330−16339.

6. Seoa J H, Nakayab H, Takeuchib Y, Fanc Z, Hikosaka H. Broad Temperature Dependence, High Conductivity, and Structure-Property Relations of Cold Sintering of LLZO-based Composite Electrolytes. J. Eur. Ceram. Soc. 2020; 40: 6241-6248.

7. Kamaya N, Homma K, Yamakawa Y, Hirayama1 M, Kanno R, Yonemura M, Kamiyama T, Kato Y, Hama S, Kawamoto K Mitsui. A Lithium Superionic Conductor. Nat. Mater. 2011; 10: 682-686.

8. Wang P, Liu H, Patel S, Feng X Y, Chien P H. Fast Ion Conduction and Its Origin in $Li_{6-x}PS5_{-x}Br_{1+x}$. Chem. Mater. 2020; 32: 3833−3840.

9. Zhu Y, He X, Mo Y, Prinz N, Eickhoff H, Minafra N. First Principles Study on Electrochemical and Chemical Stability of Solid Electrolyte-Electrode Interfaces in All-Solid-State Li-Ion Batteries. J. Mater. Chem, A. 2016; 4: 3253−3266.

10. Feng X, Chien P H, Wang Y, Patel S, Wang P B. Enhanced Ion Conduction by Enforcing Structural Disorder in Li-Deficient Argyrodites $Li_{6-x}PS_{5-x}Cl_{1+x}$. Energy Stor. Mater. 2020; 30: 67-73.

11. Ohno S, Helm B, Fuchs T, Dewald G, Wang M A. Further Evidence for Energy Landscape Flattening in the Superionic Argyrodites $Li_{6+x}P_{1-x}M_xS_5I$ (M = Si, Ge, Sn). J. Mater. Chem. 2019; 31: 4936-4944.

12. Arnold W, Buchberger D A, Li Y, Sunkara M, Druffel D T. Halide Doping effect on Solvent-Synthesized Lithium Argyrodites Li_6PS_5X (X= Cl, Br, I) Superionic Conductors. J. Power Sources. 2020; 464: 228158.

13. Zhou L, Assoud A, Zhang Q, Wu X, Nazar L F. New Family of Argyrodite Thioantimonate Lithium Superionic Conductors. J. Am. Chem. Soc. 2019; 141: 19002-19013.

14. Wang Z, Jiang Y, Wu J, Jiang Y, Huang S S. Reaction Mechanism of Li_2S-P_2S_5 System in Acetonitrile Based on Wet Chemical Synthesis of $Li_7P_3S_{11}$ Solid Electrolyte. Chem. Eng. J. 2020; 393: 124706.

15. Liang J, Chen Xi N, X Li Li, R K, Adair K R. $Li_{10}Ge(P_{1-x}Sb_x)_2S_{12}$ Lithium-Ion Conductors with Enhanced Atmospheric Stability. Chem. Mater. 2020; 32: 2664-2672.

16. Ahmad N, Zhou L, Faheem M, Tufail M K, Yang L. Enhanced Air-Stability and High Li-Ion Conductivity of $Li_{6.988}P_{2.994}Nb_{0.2}S_{10.934}O_{0.6}$ Glass-Ceramic Electrolyte for All-Solid-State Lithium-Sulfur Batteries. ACS Appl. Mater. Interfaces. 2020; 12: 21548-21558.

17. Bron P, Johansson S, Zick K, Günne J S, Dehnen D S. $Li_{10}SnP_2S_{12:}$ An Affordable Lithium Superionic Conductor. J. Am. Chem. Soc. 2013; 135: 15694−15697.

18. Vinado C, Wang S, He Y, Xiao X, Li Y, Wang C M. Electrochemical and Interfacial Behavior of All Solid-State Batteries using $Li_{10}SnP_2S_{12}$ Solid Electrolyte. J. Power Sources. 2018; 396: 824-830.

19. Nam K, Chun H, Hwang J, Han B. First-Principles Design of Highly Functional Sulfide Electrolyte of $Li_{10-x}SnP_2S_{12-x}Cl_x$ for All Solid-State Li-Ion Battery Applications. ACS Sustainable Chem. Eng. 2020; 3321−3327.

20. Sun Y, Suzuki K, Hori S, Hirayama M, Kanno R. Superionic Conductors: $Li_{10+\delta}[SnySi_{1-y}]_{1+\delta}P_2\delta S_{12}$ with a $Li_{10}GeP_2S_{12}$-type Structure in the Li_3PS_4–Li_4SnS_4–Li_4SiS_4 Quasi-ternary System. Chem. Mater. 2017; 29: 5858-5864.

21. Kato Y, Hori S, Saito T, Suzuki K, Hirayama M, Mitsui M. High-Power All-Solid-State Batteries using Sulfide Superionic Conductors. Nat. Energy. 2016; 16030.

22. Inagaki M, Suzuki K, Hori S, Yoshino K, Matsui N, Yonemura M. Conduction Mechanism of $Li_{10}GeP_2S_{12}$-Type Lithium Superionic Conductors in a Li−Sn−Si−P−S System. Chem. Mater. 2019; 31: 3485-3490.

23. Hori S, Taminato S, Suzuki K, Hirayama M, Kato Y, Kanno R. Structure–Property Relationships in Lithium Superionic Conductors Having $Li_{10}GeP_2S_{12}$-Type Structure. Acta Cryst. 2015; 71: 727-736.

24. Bron P, Dehnen S, Roling B. $Li_{10}Si_{0.3}Sn_{0.7}P_2S_{12}$ – A Low-Cost and Low-Grain-Boundary Resistance Lithium Superionic Conductor. J. Power Sources. 2016; 329: 530-535.

25. Kuhn A, Gerbig O, Zhu C, Falkenberg F. Maier J, Lotsch BV. A New Ultrafast Superionic Li-Conductor: Ion Dynamics in $Li_{11}Si_2PS_{12}$ and Comparison with Other Tetragonal LGPS-Type Electrolyte. Phys. Chem. Chem. Phys. 2014; 16: 14669-74.

26. Krauskopf T, Culver S P, Zeier W G. The Bottleneck of Diffusion and Inductive Effects in $Li_{10}Ge_{1-x}Sn_xP_2S_{12}$. Chem. Mater. 2018; 30: 1791-1798.

27. Culver S P, Squires A G, Minafra N, Armstrong C W.F, Krauskopf T. Evidence for a Solid-Electrolyte Inductive Effect in the Superionic Conductor $Li_{10}Ge_{1-x}Sn_xP_2S_{12}$. J. Am. Chem. Soc. 2020; 142: 21210-21219.

28. Stoffler H, Zinkevich T, Yavuz M, Hansen A L, Knapp M, Bednarčík. Amorphous versus Crystalline Li_3PS_4: Local Structural Changes During Synthesis and Li Ion Mobility. J. Phys. Chem. C. 2019; 123: 10280-10290.

29. Preefer M B, Grebenkemper J H, Schroeder F, Bocarsly J D, Pilar K. Rapid and Tunable Assisted-Microwave Preparation of Glass and Glass-Ceramic Thiophosphate "$Li_7P_3S_{11}$" Li-Ion Conductors. ACS Appl. Mater. 2019; 11: 42280-42287.

30. Hassouna J, Verrellia R, Realea P, Paneroa S, Mariotto G. A Structural, Spectroscopic and Electrochemical Study of a Lithium Ion Conducting $Li_{10}GeP_2S_{12}$ Solid Electrolyte. J. Power Sources. 2013; 229: 117-122.

31. Yang K, Dong J, Zhang L, Li Y, Wang L L. Dual Doping: An Effective Method to Enhance the Electrochemical Properties of $Li_{10}GeP_2S_{12}$ - Based Solid Electrolytes. J. Am. Ceram. Soc. 2016; 98: 3831-3835.

32. Minami K, Hayashi A, Tatsumisago M. Preparation and Characterization of Lithium Ion Conducting Li_2S-P_2S_5-GeS_2 Glasses and Glass-Ceramics, J Non Cryst Solids. 2010; 356: 2666-2669.

33. Kanazawa, Yubuchi S, Hotehama C, Otoyama M, Shimono S. Mechanochemical Synthesis and Characterization of Metastable Hexagonal Li_4SnS_4 Solid Electrolyte. Inorg. Chem. 2018; 57: 9925-9930.

34. Zhang Z, Zhang J, Sun Y Jia H, $Li_{4-x}Sb_xSn_{1-x}S_4$ Solid Solutions for Air-Stable Solid Electrolytes. J. Energ. Chem. 2020; 41: 171-176.

35. Seino Y, Ota T, Takada K, Hayashi A, Tatsumisago M. A Sulphide Lithium Super Ion Conductor is Superior to Liquid Ion Conductors for Use in Rechargeable Batteries. Energy Environ. Sci. 2014; 7(2); 627-631.

36. Qiao A, Tao H, Yue Y. Enhancing ionic conductivity in Ag_3PS_4 via mechanical amorphization. Journal of Non-Crystalline Solids. 2019; 521: 119476.

37. Wang L, Zhao Y, Thomas M L, Byon H R. In Situ Synthesis of Bipyramidal Sulfur with 3D Carbon Nanotube Frame-work for Lithium−Sulfur Batteries. Adv. Funct. Mater. 2014; 24: 2248−2252.

38. Huang B, Yao X, Huang Z, Guan Y, Jin Y, Xu X. Li_3PO_4-doped $Li_7P_3S_{11}$Glass-Ceramic Electrolytes with Enhanced Lithium Ion Conductivities and Application in All-Solid-State Batteries. J. Power Sources. 2015; 284: 206−211.

39. Hayashi A, Sakuda A, Tatsumisago M. Development of Sulfide Solid Electrolytes and Interface Formation Processes for Bulk-Type All-Solid-State Li and Na Batteries. Front. Energy Res. 2016; 4: No. 25.

40. Zhang Y, Chen R, Liu T, Shen Y, Lin Y, Nan C W. High Capacity, Superior Cyclic Performances in All-Solid-State Lithium-Ion Batteries Based on $78Li_2S$-$22P_2S_5$Glass-Ceramic Electrolytes Prepared Via Simple Heat Treatment. ACS Appl. Mater. Interfaces. 2017; 9: 28542−28548.

41. Zhang Y, Chen R, Liu T, Xu B, Zhang X, Li L, Lin Y, Nan C W. Shen Y. High Capacity and Superior Cyclic Performances of All-Solid-State Lithium-ion Batteries Enabled by a Glass-Ceramic Solo. ACS Appl. Mater. Interfaces. 2018; 10: 10029−10035.

42. Zhang Q, Yao X, Mwizerwa J P, Huang N, Wan H, Huang Z, Xu X. FeS Nanosheets as Positive Electrodes for All-Solid-State Lithium Batteries. Solid State Ion. 2018; 318: 60−64.

List of Figure Captions

Fig. 1(a) X-ray diffraction diagram of (1+*x*) Li_3PS_4–(2-*x*) Li_4SnS_4 (*x*=0, 0.5, 1, 1.5, 1.7) after 30h of mechanical grinding. (b) The XRD patterns of the $2.5Li_3PS_4$–$0.5Li_4SnS_4$ (*x*=1.5) after 30h ball milling and 72h heat treatment at different temperatures, the standard red and black lines represent $Li_{10}SnP_2S_{12}$, Li_3PS_4 standard XRD, respectively.

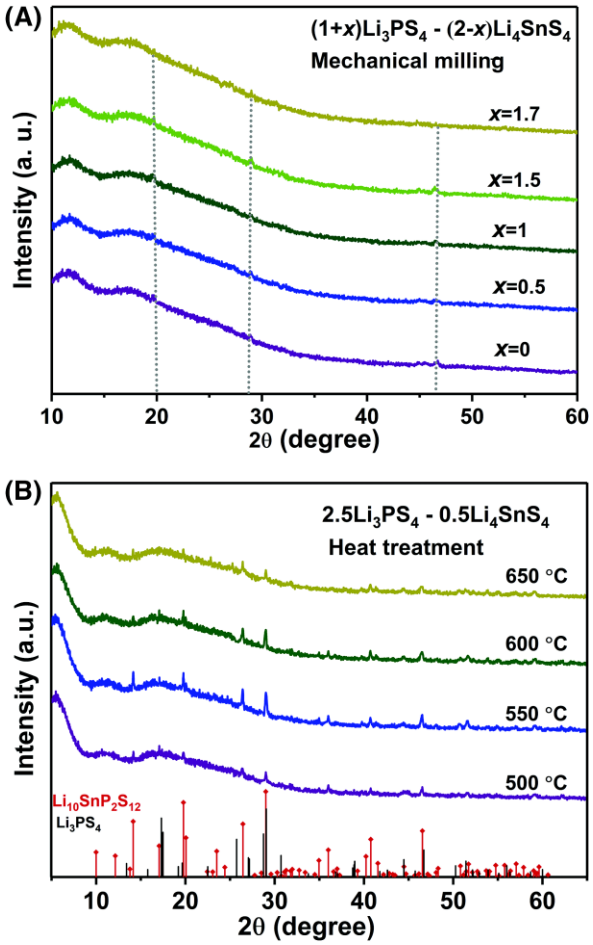

Fig. 2(a) Raman spectrum of all samples (1+*x*) Li_3PS_4–(2-*x*) Li_4SnS_4 after mechanical grinding with 30h. (b) Raman spectra of the $2.5Li_3PS_4$–$0.5Li_4SnS_4$ (*x*=1.5) sample after further 72h heat treated from 500°C to 650°C.

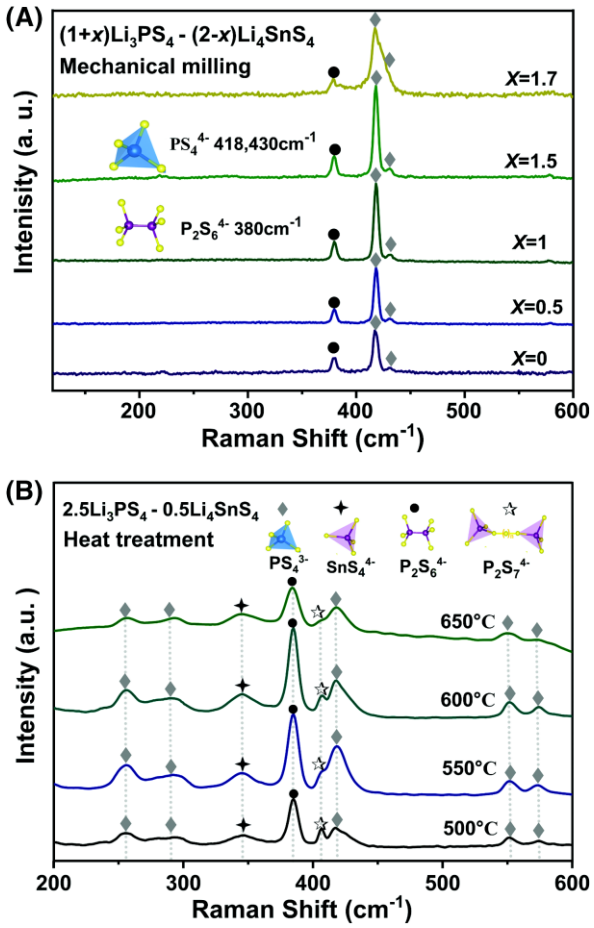

Fig. 3(a) Impedance of (1+*x*) Li_3PS_4–(2-*x*) Li_4SnS_4 SSE by milling. The inset corresponds to an enlarged view of impedance and analog circuits. (b) Typical impedance plots of $2.5Li_3PS_4$–$0.5Li_4SnS_4$ (*x*=1.5) treated at temperatures from 500°C to 650°C. The inset corresponds to impedance magnification and analog circuits. (c) Ionic conductivity dependence of *x* values and different heat treatment temperatures. The inset shows the conductivity of $2.5Li_3PS_4$–$0.5Li_4SnS_4$ (*x*=1.5) SSE under different heat treatment temperatures. (d) Direct current polarization of the SS/$2.5Li_3PS_4$–$0.5Li_4SnS_4$/SS cell at different voltages. The inset exhibits a linear fitting of the electronic impedance values of 2.5Li3PS4–0.5Li4SnS4 after heat treatment at 550°C. (e) Impedance of 550°C heat-treated $2.5Li_3PS_4$–$0.5Li_4SnS_4$ SSE measured from 30°C to 100°C. (f) Arrhenius curves of $2.5Li_3PS_4$–$0.5Li_4SnS_4$ SSE after milling and heat treatment at 500, 550, 600, 650°C.

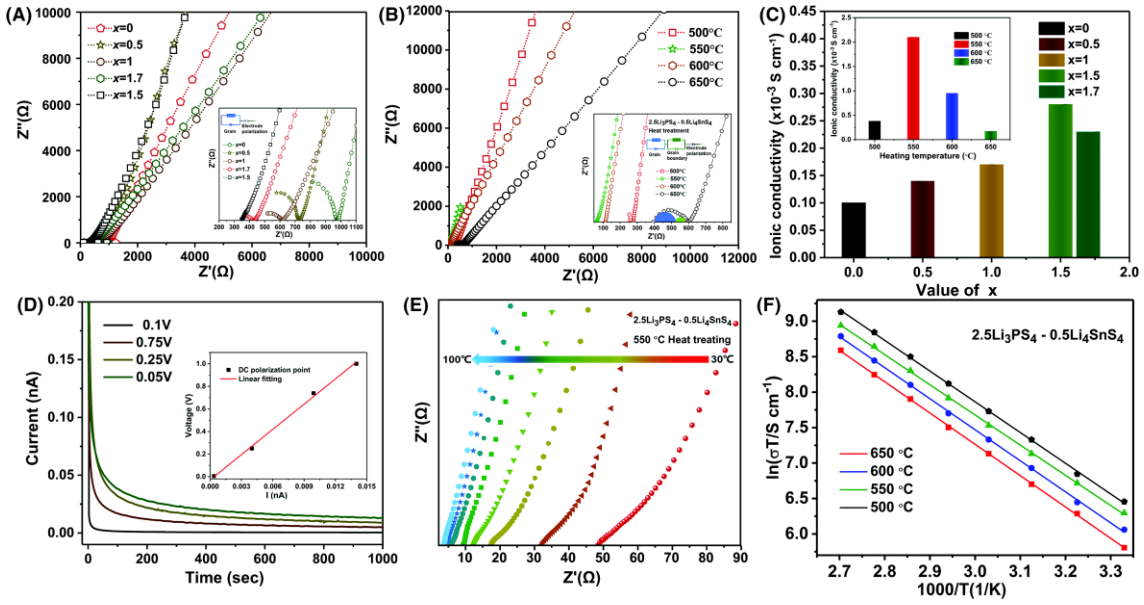

Fig. 4 Cyclic voltammetry (CV) curve of Li/2.5Li_3PS_4–0.5Li_4SnS_4/SS cell with the voltage range from – 0.1 to 5 V at 1 mV s^{-1}.

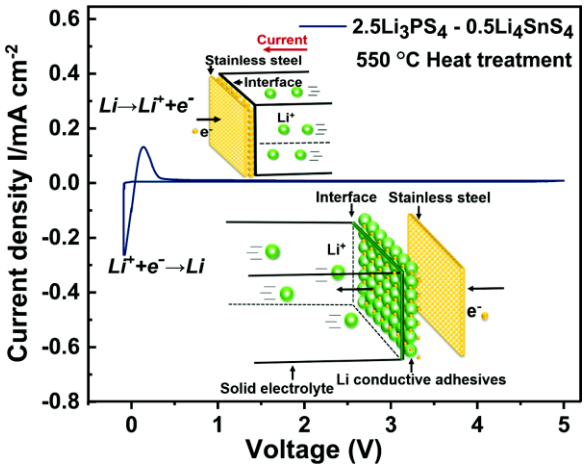

Fig. 5(a) Model system of pristine $Li_{10}SnP_2S_{12}$ crystal structure from the online database with a space group of $P4_2/mc$. Yellow spheres for S, purple spheres for Sn and blue spheres for P. (b) The simulated jumping sites and transportation route of Li^+ ions. (c) Schematic diagram of the coulomb interaction between S and Li with different M–S (M=Sn, P) bonding structure.

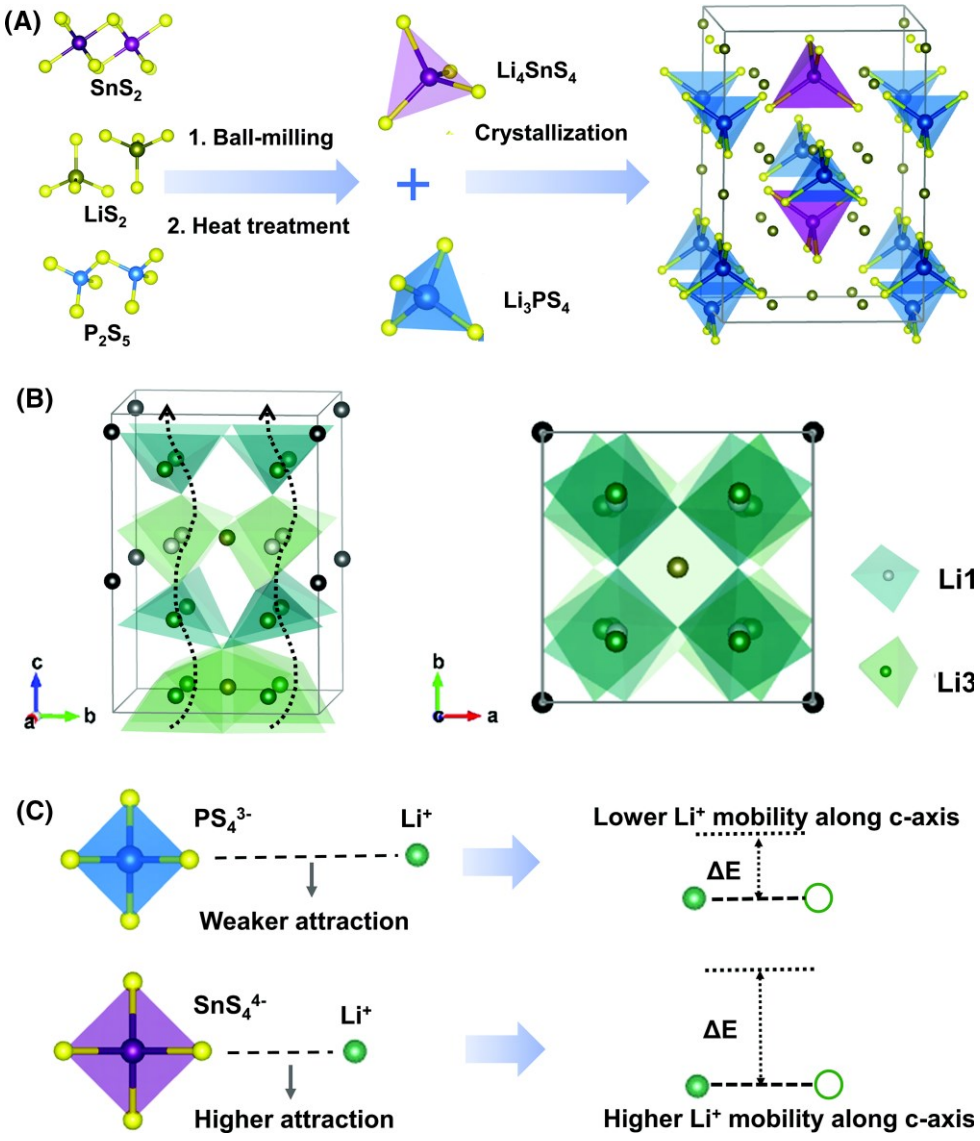

Fig. 6(a) Schematic diagram of LCO/2.5Li_3PS_4–0.5Li_4SnS_4/Li all-solid-state battery. (b) Cyclic performance of the battery under 40 mA g^{-1}. (c) Charge−discharge profiles of the battery for the 1st, 5th, 10th, 15th, 20th and 25th cycles. (d) Impedance plots for the cells after the first and the 25th cycle.